

Lawrence Berkeley National Laboratory

LBL Publications

Title

Carbide Formation in Refractory Mo₁₅Nb₂₀Re₁₅Ta₃₀W₂₀ Alloy under a Combined High-Pressure and High-Temperature Condition

Permalink

<https://escholarship.org/uc/item/88d2k1bp>

Journal

Entropy, 22(7)

ISSN

1099-4300

Authors

Zhang, Congyan
Bhandari, Uttam
Zeng, Congyuan
et al.

Publication Date

2020-06-01



DOI

10.3390/e22070718

Peer reviewed

Article

Carbide Formation in Refractory $\text{Mo}_{15}\text{Nb}_{20}\text{Re}_{15}\text{Ta}_{30}\text{W}_{20}$ Alloy under a Combined High-Pressure and High-Temperature Condition

Congyan Zhang ¹, Uttam Bhandari ¹, Congyuan Zeng ², Huan Ding ², Shengmin Guo ² , Jinyuan Yan ³ and Shizhong Yang ^{1,*} 

¹ Department of Computer Science, Southern University and A&M College, Baton Rouge, LA 70813, USA; congyan_zhang@subr.edu (C.Z.); uttam_bhandari_00@subr.edu (U.B.)

² Department of Mechanical and Industrial Engineering, Louisiana State University, Baton Rouge, LA 70803, USA; czeng8@lsu.edu (C.Z.); hding3@lsu.edu (H.D.); sguo2@lsu.edu (S.G.)

³ Lawrence Berkeley National Laboratory, Berkeley, CA 94720, USA; jyan@lbl.gov

* Correspondence: Shizhong_yang@subr.edu; Tel.: +225-771-3113

Received: 11 June 2020; Accepted: 26 June 2020; Published: 28 June 2020



Abstract: In this work, the formation of carbide with the concertation of carbon at 0.1 at.% in refractory high-entropy alloy (RHEA) $\text{Mo}_{15}\text{Nb}_{20}\text{Re}_{15}\text{Ta}_{30}\text{W}_{20}$ was studied under both ambient and high-pressure high-temperature conditions. The x-ray diffraction of dilute carbon (C)-doped RHEA under ambient pressure showed that the phases and lattice constant of RHEA were not influenced by the addition of 0.1 at.% C. In contrast, C-doped RHEA showed unexpected phase formation and transformation under combined high-pressure and high-temperature conditions by resistively employing the heated diamond anvil cell (DAC) technique. The new FCC_L1₂ phase appeared at 6 GPa and 809 °C and preserved the ambient temperature and pressure. High-pressure and high-temperature promoted the formation of carbides Ta₃C and Nb₃C, which are stable and may further improve the mechanical performance of the dilute C-doped alloy $\text{Mo}_{15}\text{Nb}_{20}\text{Re}_{15}\text{Ta}_{30}\text{W}_{20}$.

Keywords: high-entropy alloy; compression deformation; synchrotron x-ray diffraction; diamond anvil cell; high-pressure and high-temperature property

1. Introduction

High-entropy alloys (HEAs), which are considered as a new class of advanced metallic materials, are drawing increasing attention because of their promising properties [1–3], such as high strength at both room temperature and elevated temperatures [4,5], exceptional ductility [6], and toughness [7]. HEAs were initially defined as alloys containing five or more elements with equal or near-equal concentrations [8], while the later studies expended HEAs to include minor elements [9]. Many studies on HEAs were motivated by the possibility that properties may be tunable based on the elements contained in the HEAs. For example, Al-based HEAs [10–13] were studied for application on aircraft engines and nuclear reactors because of their low densities. On the other hand, because of the high melting temperature and high hardness of W and Re, HEAs that contained W or Re were expected to maintain advanced mechanical properties for high-temperature applications [5,14].

Beside the contained elements in HEA, doping with interstitial elements such as carbon to HEA has been announced to be an effective way to improve the mechanical properties [15–22]. The tensile yield strength of CoCrFeMnNi could increase from 371 MPa to 792 MPa just by adding 3.0 at.% C [22]. It was reported that the doped C atoms may have strong interactions with elements in HEA to form carbides, which usually lead to higher strength. As expected, both the yield strength and the ultimate tensile strength increase with the carbon content increasing in CoCrFeMnNi [22]. By analogy, the increase of both

compressive strength and the plasticity of the $\text{Mo}_{0.5}\text{NbHf}_{0.5}\text{ZrTi}$ refractory HEA (RHEA) was attributed to the formation of carbides (MC with $M = \text{Nb, Hf, Zr, and Ti}$), when the concentration of C was only 0.3 at.%, a dilute doping case [20].

The formation of carbides might be influenced by multiple aspects, like concentration of C, and atomic interactions between C and other elements in HEA. The pressure and temperature could also affect the formation of carbides. However, studying the interstitial C alloying HEAs under both high-pressure and high-temperature is a great challenge. The technique of synchrotron radiation, combined with double-sided laser heating or resistive heating, has become a unique method for combined high-temperature and high-pressure studies [23]. The laser-heated diamond anvil cell (LHDAC) [24–26] has become an important tool, which can easily generate high pressure by compressing small samples between two opposing diamond culets. However, the lack of temperature measurement accuracy is an ongoing problem [25]. Resistively heated diamond anvil cell (DAC) [27] controls the temperature by mounting an electrical heater with adjustable voltage and current out of the DAC body. In this case, the temperature inside DAC body can be easily controlled and measured.

2. Materials and Methods

The first group of tests was conducted on samples prepared under high temperature via an arc-melter at a low pressure. $\text{Mo}_{15}\text{Nb}_{20}\text{Re}_{15}\text{Ta}_{30}\text{W}_{20}$ (master alloy), which was reported to have high hardness [28], and master alloy with dilute C-doped at 0.1 at. % ($\text{C}_{0.1}$ -alloy) samples were synthesized using the arc melting method (Edmund Bühler /MAM-1) under an argon atmosphere. C, Mo, Nb, Re, Ta, and W powders with purity of more than 99.5 % were mixed inside a polystyrene mill jar for 15 min and then pressed in a uniaxial die at 350 MPa pressure. To ensure chemical homogeneity, the melted ingots were inverted and remelted four times under the arc. To melt the samples, an arc melter was used under an argon atmosphere. As metal powders can be easily ejected from the arc region, metal powders were first mixed and then pressed in a uniaxial stainless-steel die to form disk shaped blocks. After loading the disk-shaped samples into the arc-melter processing chamber, the arc-melter vacuum system would pull vacuum and then high purity argon gas would refill the chamber. Typically, the evacuation/refill process was repeated at least three times to ensure a low residual oxygen level. With a proper chamber argon pressure (~ 0.3 bar), the arc was initiated to melt the sample on a water-cooled copper plate (no crucible was used). After complete melting, the arc was kept on for about 10 s. Then, the melted sample solidifies to form a button shaped ingot. This ingot would be flipped over, and the arc melting process was repeated for three more times. The repeated melting would ensure the chemical homogeneity within the ingots. Due to the repeated evacuation/refill process and the use of high purity Ar gas as the protective gas, the oxidation is kept to a minimum and thus not considered in this study. The crystal structure, microstructure, and hardness of $\text{C}_{0.1}$ -alloy and master alloy samples (synthesized using the same arc melting method) were examined to investigate the effects of C doping to the structural and mechanical properties of the alloy. The crystal structure of both types of samples were analyzed by a PANalytical Empyrean x-ray diffraction (XRD) system with 2 theta scans range from 20–120 degrees. The wavelength of the incident x-ray was 1.5406 Å. The microstructures of both types of samples were studied using scanning electron microscopy (SEM), and the chemical compositions were analyzed. The hardness characterization was performed with a SUN-TEC CM-802AT (V/K) hardness-testing machine. Five indents were conducted for each testing load to ensure the repeatability of the results. The space between adjacent indents was over three times the indent diagonal length.

Further studies on performance of $\text{C}_{0.1}$ -alloy sample under high-temperature and high-pressure were performed by using the resistive heated synchrotron DAC technique. The DAC XRD data under high-pressure and high-temperature were collected at beamline 12.2.2 at the Advanced Light Source (ALS), Lawrence Berkeley National Laboratory (LBNL) with an x-ray wavelength of 0.4959 Å. CeO_2 was used as the standard material to calibrate the sample-detector distance and detector orientation and Au powder was used for the pressure calibration. The testing powders were loaded

into the resistor heated DAC with pressure-generating membrane. The pressure was controlled by pressure-generating membrane, and the temperature was controlled by an electrical heater with adjustable voltage and current, which was mounted out of DAC body. The DAC main body was cooled by a circulating liquid. The performance of $C_{0.1}$ -alloy under the combined high-pressure and high-temperature condition was studied by the high-pressure and high-temperature synchrotron XRD experiment. $C_{0.1}$ -alloy mixed with Au sample was firstly compressed at room temperature until 6 GPa, then was heated from room temperature to ~ 1000 °C in 10 h while pressure kept at 6 GPa. In this case, the performance of $C_{0.1}$ -alloy under high-pressure low-temperature (high P/low T) and under high-pressure high-temperature (high P/high T) could be investigated [29]. At last, the sample was cooled to room temperature in 2 h. The diffraction images at room temperature were initially analyzed by Dioptas [30] to determine the pressure by fitting to the standard Au diffraction peaks. The diffraction images under the combined high-pressure and high-temperature were refined to remove the background noise by material analysis [31] using diffraction (MAUD) software.

3. Results

3.1. Phase and Microstructure at Low-Pressure

The XRD patterns of both master alloy and $C_{0.1}$ -alloy are shown in Figure 1a. As shown in the figure, only body center cubic (BCC) peaks were detected in both samples, indicating stable single BCC crystals. No carbide was obtained in $C_{0.1}$ -alloy under ambient pressure and temperature (low P/low T) based on the XRD observation. Considering that samples were already melted several times during synthesis but no XRD-peaks-related carbide were obtained, it is concluded that carbide could not be formed under ambient pressure and high temperature (low P/high T). Moreover, the peaks with the same crystallographic plane were in the plot, which is due to the almost identical lattice constants of both crystals, apart from the peaks at planes (220) and (310). The small differences in planes (220) and (310) are likely caused by the diffraction features of the segregations from the matrix in Figure 2. The doped C elements would not induce any noticeable changes on the lattice constant. According to Bragg's law [32], the lattice parameters of master alloy and $C_{0.1}$ -alloy were both determined to be 3.210 Å. Because of the low concentration and small atom size of C, the effect from doped C to lattice constant of HEA is negligible. Similar observations on HEA such as $Mo_{0.5}NbHf_{0.5}ZrTi$ [20] and $CoCrFeMnNi$ [15] were reported.

SEM microstructure of master alloy and $C_{0.1}$ -alloy are shown in Figure 1b,c, respectively. Black dots in the SEM microstructures of the samples show the existence of segregations. No obvious morphological changes were observed in the SEM images due to the addition of low concentration of C. SEM second electron images and SEM energy-dispersive spectroscopy (EDS) elemental mapping of $C_{0.1}$ -alloy are shown in Figure 2 to demonstrate the chemical compositions of alloys. C element could not be identified using XRD/SEM techniques because of its low concentration. It has been identified that all regions in the SEM images are the BCC phase, which confirmed the analysis on XRD patterns that no carbide formed in $C_{0.1}$ -alloy. The EDS mapping images show that the dark areas were enriched in Nb, Mo, and Ta elements but depleted in W and Re.

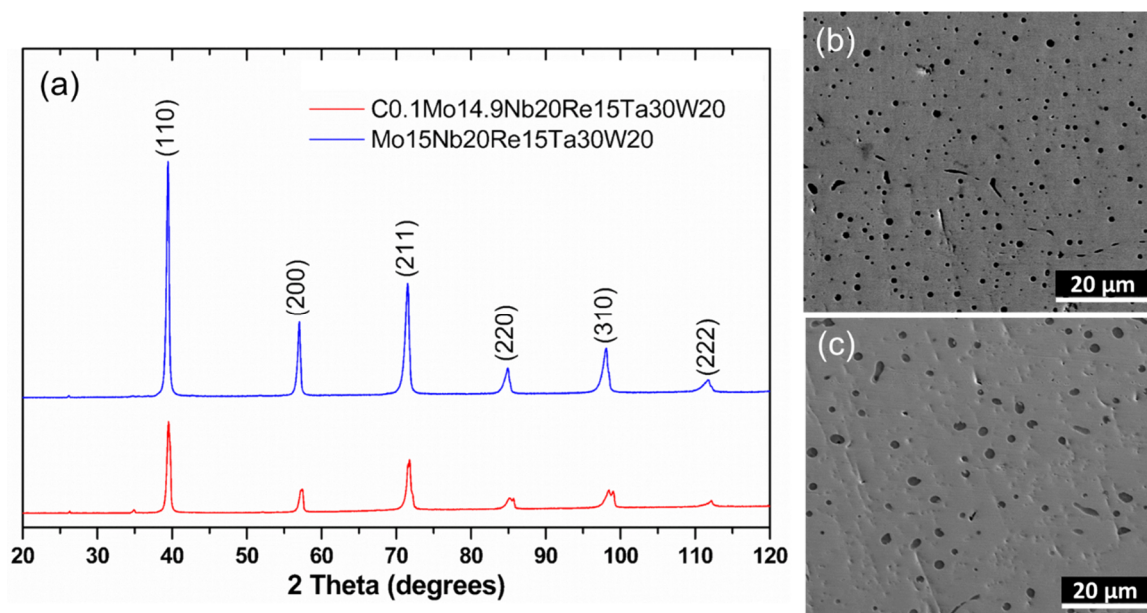


Figure 1. (a) XRD pattern of master alloy and $C_{0.1}$ -alloy, and SEM images showing microstructures of (b) master alloy and (c) $C_{0.1}$ -alloy.

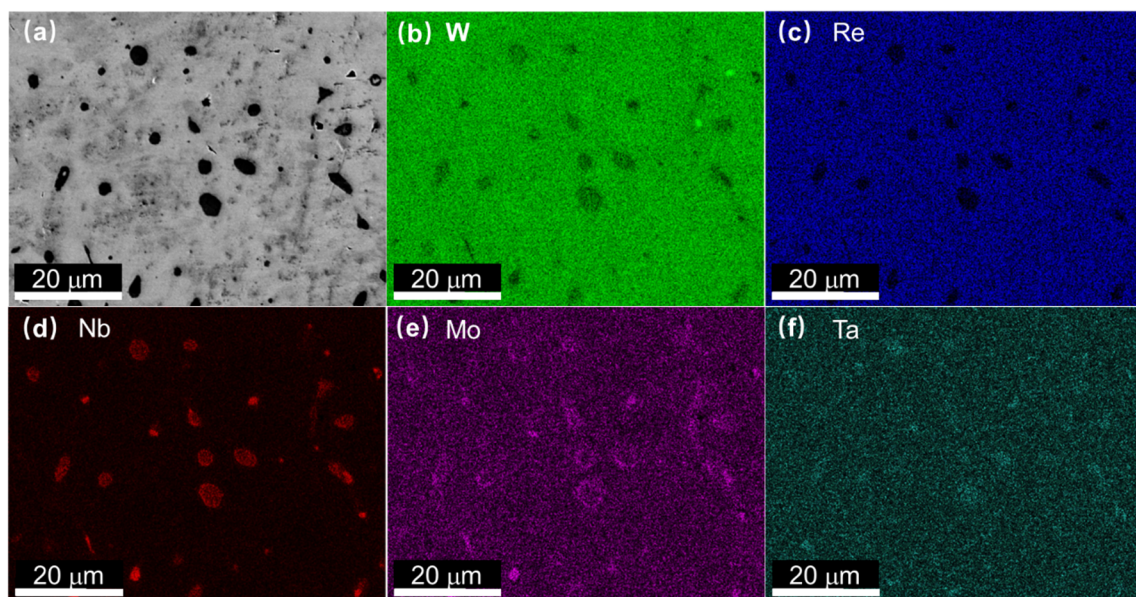


Figure 2. (a) SEM image of $C_{0.1}$ -alloy, energy-dispersive spectroscopy (EDS) mapping images for (b) W, (c) Re, (d) Nb, (e) Mo, and (f) Ta.

Based on the EDS composition analysis of $C_{0.1}$ -alloy in 9 selected areas, the average chemical compositions of C, Mo, Nb, Re, Ta, and W are listed in Table 1. As the reference, the chemical compositions in master alloy are also listed. The compositions of elements in both samples are very close. However, the Vickers micro hardness for both samples, which were tested at five different spots on the sample, showed a noticeable difference, as listed in the end of Table 1. The hardness values of both samples were obtained by using three different loads (gf)—100, 500, and 2000, respectively. It is clearly shown that Vickers hardness of master alloy reduced with the increase of load, while hardness of $C_{0.1}$ -alloy kept about the same under different loads. This indicates that the interstitial C atoms in the material help to pin the dislocations, and to restrain the movement of those dislocations. Several methods have been reported to calculate the Vickers hardness of alloys [28,33]. While the

concentration of C in C_{0.1}-alloy is too small to calculate by DFT, the role of mixture was employed to estimate the influence of C to the master alloy. The estimated Vickers hardness of master alloy is 8.33 GPa, and Vickers hardness of C_{0.1}-alloy is 8.27 GPa. Both experimental observation and theoretical estimation show that influence of low concentration C to the hardness of alloys is very small.

Table 1. The chemical compositions (at.%) of master alloy (alloy) and C_{0.1}-alloy (C-doped) and the Vickers micro hardness of both samples.

Sample	C	Mo	Nb	Re	Ta	W	Hardness		
							100 gf	500 gf	2000 gf
alloy	-	14.43 ± 0.17	22.74 ± 0.38	15.29 ± 0.09	26.66 ± 0.19	20.90 ± 0.19	6.451 ± 0.140	6.035 ± 0.303	5.400 ± 0.213
C-doped	0.06	14.32 ± 0.41	22.63 ± 0.54	18.12 ± 0.28	26.44 ± 0.32	18.43 ± 0.26	5.826 ± 0.104	5.905 ± 0.086	5.749 ± 0.203

3.2. C_{0.1}-Alloy under High P/low T and High P/high T

In situ XRD patterns of the C_{0.1}-alloy/Au mixtures from low P/low T to high P/low T condition are shown in Figure 3a, where the XRD peaks of Au are marked. At room temperature and no applied pressure, C_{0.1}-alloy was identified to have only a BCC phase with a lattice constant of 3.211 Å by DAC XRD, which is consistent with the observation of PANalytical Empyrean XRD. No new peak appeared during compression, indicating the stability of the BCC phase under a pressure up to ~6 GPa. No carbide was obtained under high P/low T condition. It is also clearly shown that all diffraction peaks shift to larger 2θ angles with increasing pressure. The corresponding *d*-spaces for (111), (200), (211), and (220) planes of C_{0.1}-alloy as the functions of pressure at room temperature are shown in the left panel of Figure 4. *d*-spaces decrease as increasing pressure, indicating decreasing of lattice parameter. At 6 GPa, *d*-spaces of C_{0.1}-alloy are about 0.5% smaller than that at 0 GPa.

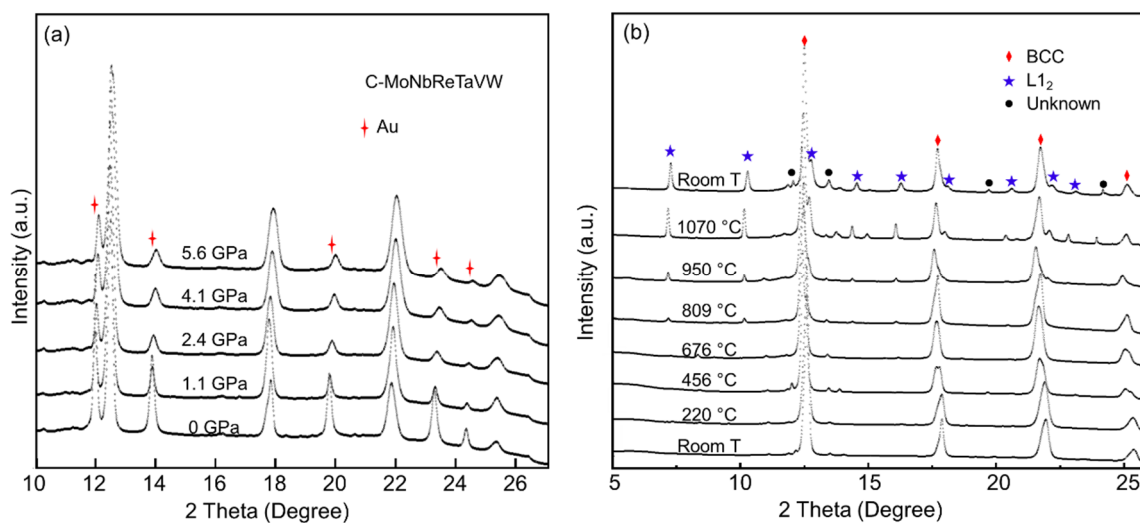


Figure 3. (a) XRD patterns of C_{0.1}-alloy/Au mixture when pressure increased from 0 GPa to ~6 GPa. The corresponding pressures are marked on the top of each XRD pattern. XRD patterns of Au are marked by the red stars. (b) XRD patterns of C_{0.1}-alloy/Au mixture with various temperatures when the pressure was 6 GPa. The corresponding temperatures are marked on the top of each XRD pattern. XRD patterns of body center cubic (BCC) phase are marked by red diamond; L₁₂ phase, blue star; unknown, black dots.

After the sample was compressed to 6 GPa, the temperature was increased by applying the heater mounted out of DAC body. XRD patterns of C_{0.1}-alloy/Au mixture from high P/low T to high P/high T are shown in Figure 3b. With the increase of temperature, atomic vibration increased, which lead to the increase of lattice constant. Consequently, the XRD peaks shift to the smaller angles while temperature increases. C_{0.1}-alloy was found to have only BCC phase below 676 °C. A group of nonignorable peaks

marked as blue star in Figure 3b appeared when the temperature increased to 809 °C, representing the formation of new phase. This new phase was identified to be the L₁₂ phase by QualX 2.0 [34], similar XRD peak of carbides with L₁₂ phase in AlCoCrFeNi was reported in Ref. [35]. Intensity of these new peaks became stronger when the temperature increased to above 1000 °C, indicating higher concentration of L₁₂ phase with increasing temperature. The new peaks existed even when samples were cooled back to room temperature, which indicated nonreversible phase transition happened in BCC C_{0.1}-alloy under high pressure.

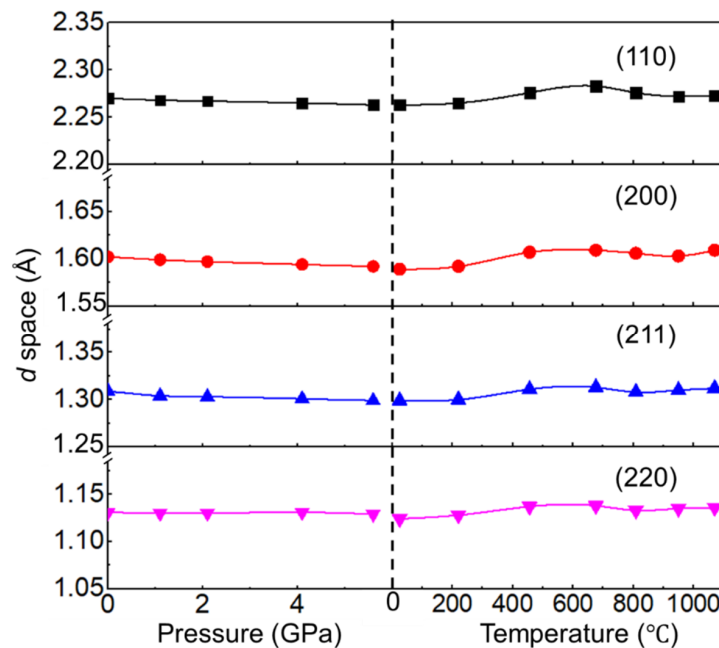


Figure 4. *d*-space as the function of pressure at room temperature (**left**) and *d*-space as the function of temperature at 6 GPa (**right**).

The *d*-spaces for (111), (200), (211), and (220) planes of C_{0.1}-alloy as the functions of temperature with pressure kept at 6 GPa are shown in the right panel of Figure 4. *d*-spaces increase as temperature increases to 676 °C. The drop of *d*-space for all BCC planes was found when the temperature increased from 676 °C to 809 °C, indicating the formation of new phase in this temperature range. The phase transition leads to change of elements configuration in BCC phase. As a consequence, over the temperature range of 676 °C to 809 °C, the *d*-spaces of BCC crystal were smaller than those when the temperature was 676 °C. After 809 °C, *d*-spaces increased as temperature increased to 1070 °C.

Combining the synthesis and characterization process, C_{0.1}-alloy was treated through low P/high T, low P/low T, high P/low T, and high P/high T. Carbides were obtained under high P/high T and preserved back to the ambient temperature and pressure. The performance indicates that applied pressure and temperature could promote the formation of carbides when the doped concentration is low.

4. Discussion

To analyze the component of L₁₂ phase, the electronegativity difference ($\Delta\chi_r$) and chemical enthalpy of mixing (ΔH_{mix}) of binary equiatomic alloys according to Miedema's model [36] between elements in C_{0.1}-alloy were compared in Table 2. C-Ta pair has largest electronegativity difference, indicating strongest attractive interaction between C and Ta to form binary compounds. Moreover, electronegativity differences of C-Nb and C-Re are also relatively large compared with other pairs, which shows that C-Nb and C-Re binary compounds are also easily formed. The chemical mixing enthalpy listed in Table 2b shows that the pairs that contain C elements are much more negative than others, which indicates that binary intermetallic

phase between C and other elements may easily form. Strongest binding strength exists between C and Nb, followed by Re, Mo, Ta, and W.

Table 2. (a) The electronegativity difference $\Delta\chi_r$ (by Pauling scale) and (b) values of chemical mixing enthalpy ΔH_{mix} (kJ/mol) of atomic pairs between elements for alloy C_{0.1}-alloy.

	(a)						
(b)	C	Mo	Nb	Re	Ta	W	Elements
C	-	-67	-102	-101	-60	-42	C
Mo	0.39	-	-6	-7	-5	0	Mo
Nb	0.95	0.56	-	-26	0	-8	Nb
Re	0.65	0.26	0.3	-	-24	-4	Re
Ta	1.05	0.66	0.1	0.4	-	-7	Ta
W	0.19	0.2	0.76	0.46	0.86	-	W
Elements	C	Mo	Nb	Re	Ta	W	(a)

L₁₂ phase is FCC phase with two elements (chemical formula: AB₃) in one primitive unit cell. The space group of both L₁₂ phases is $\overline{pm}3m(221)$ with Pearson symbol of cP4. The database FactSage [37] listed the phase diagram of C-based binary alloy phase diagram at zero pressure. According to the database, C-Ta and C-Nb could form FCC phase, C-Mo and C-Re could form HCP phase, and C-W could form BCC phase. By combining the electronegativity difference and chemical mixing enthalpy analysis in Table 2, the L₁₂ phase identified under high-pressure and high-temperature is likely to be Ta₃C and Nb₃C binary compounds. TaC and NbC binary compounds were reported to have unique combination of properties, such as high-melting temperature, high hardness, good high-temperature strength, and good conductivity [38–40]. These carbides are usually employed as high-temperature structural materials in the form of hard constituents in metal matrix composites.

5. Conclusions

In this work, the effect of dilute C-doped with a concentration of 0.1 at.% in RHEA master alloy was studied under both ambient pressure and high-pressure high-temperature conditions. Under low pressure, the XRD of RHEA with/without C shows the formation of pure BCC phase and lattice constant of 3.210 Å, indicating that the low concentration of C has an ignorable effect on the alloy phase and the crystal structure of RHEA. However, the doping of C has noticeable a impact on the hardness values of the RHEA. At a high pressure of 6 GPa, Ta₃C and Nb₃C Carbide with FCC_L1₂ phase appear when the temperature is above 809 °C. The carbides of Ta₃C and Nb₃C are very stable even when temperature increased to above 1000 °C. As carbides are usually shown and favorable in high-temperature structural materials in the form of hard constituents in metal matrix composites, the mechanical properties of carbon doped master alloy RHEA might be improved after a combined high-pressure and high-temperature process.

Author Contributions: Conceptualization, C.Z. (Congyan Zhang) and S.Y.; Investigation, C.Z. (Congyan Zhang), U.B., C.Z. (Congyuan Zeng), H.D., S.G., J.Y., and S.Y.; Methodology, C.Z. (Congyan Zhang) and U.B.; Resources, S.G. and J.Y.; Writing—original draft, C.Z. (Congyan Zhang); Writing—review and editing, U.B., C.Z. (Congyuan Zeng), H.D., S.G., J.Y., and S.Y. All authors have read and agreed to the published version of the manuscript.

Funding: This research was funded by U.S. Department of Energy, grant number DE-AC02-05CH11231; NSF EPSCoR CIMM project, grant number 1541079; and U.S. Department of Defense, grant number W911NF1910005.

Acknowledgments: We acknowledge the support from the Advanced Light Source at Lawrence Berkeley National Laboratory and helpful support from Dongmei Cao at Shared Instrument Facility at Louisiana State University.

Conflicts of Interest: The authors declare no conflict of interest.

References

1. Miracle, D.B.; Senkov, O.N. A critical review of high entropy alloys and related concepts. *Acta Mater.* **2017**, *122*, 448–511. [[CrossRef](#)]
2. Ye, Y.F.; Wang, Q.; Lu, J.; Liu, C.T.; Yang, Y. High-entropy alloy: Challenges and prospects. *Mater. Today* **2016**, *19*, 349–362. [[CrossRef](#)]
3. Tsai, M.-H.; Yeh, J.-W. High-entropy alloys: A critical review. *Mater. Res. Lett.* **2014**, *2*, 107–123. [[CrossRef](#)]
4. Senkov, O.N.; Wilks, G.B.; Scott, J.M.; Miracle, D.B. Mechanical properties of Nb₂₅Mo₂₅Ta₂₅W₂₅ and V₂₀Nb₂₀Mo₂₀Ta₂₀W₂₀ refractory high entropy alloys. *Intermetallics* **2011**, *19*, 698–706. [[CrossRef](#)]
5. Kang, B.; Lee, J.; Ryu, H.J.; Hong, S.H. Ultra-high strength WNbMoTaV high-entropy alloys with fine grain structure fabricated by powder metallurgical process. *Mater. Sci. Eng. A* **2018**, *712*, 616–624. [[CrossRef](#)]
6. Yao, M.J.; Pradeep, K.G.; Tسان, C.C.; Raabe, D. A novel, single phase, non-equiatomic FeMnNiCoCr high-entropy alloy with exceptional phase stability and tensile ductility. *Scr. Mater.* **2014**, *72–73*, 5–8. [[CrossRef](#)]
7. Patriarca, L.; Ojha, A.; Sehitoglu, H.; Chumlyakov, Y.I. Slip nucleation in single crystal FeNiCoCrMn high entropy alloy. *Scr. Mater.* **2016**, *112*, 54–57. [[CrossRef](#)]
8. Yeh, J.-W.; Chen, S.-K.; Lin, S.-J.; Gan, J.-Y.; Chin, T.-S.; Shun, T.-T.; Tsau, C.-H.; Chang, S.-Y. Nanostructured high-entropy alloys with multiple principal elements: Novel alloy design concepts and outcomes. *Adv. Eng. Mater.* **2004**, *6*, 299–303. [[CrossRef](#)]
9. Tong, C.-J.; Chen, Y.-L.; Yeh, J.-W.; Lin, S.-J.; Chen, S.-K.; Shun, T.-T.; Tsau, C.-H.; Chang, S.-Y. Microstructure characterization of Al_xCoCrCuFeNi high-entropy alloy system with multiprincipal elements. *Metall. Mater. Trans. A* **2005**, *36*, 881–893. [[CrossRef](#)]
10. Xu, Z.Q.; Ma, Z.L.; Wang, M.; Chen, Y.W.; Tan, Y.D.; Cheng, X.W. Design of novel low-density refractory high entropy alloys for high-temperature applications. *Mater. Sci. Eng. A* **2019**, *755*, 318–322. [[CrossRef](#)]
11. Kang, M.; Lim, K.R.; Won, J.W.; Lee, K.S.; Na, Y.S. Al-Ti-Containing lightweight high-entropy alloys for intermediate temperature applications. *Entropy* **2018**, *20*, 355. [[CrossRef](#)]
12. Youssef, K.M.; Zaddach, A.J.; Niu, C.; Irving, D.L.; Koch, C.C. A Novel Low-Density, High-hardness, high-entropy alloy with close-packed single-phase nanocrystalline structures. *Mater. Res. Lett.* **2015**, *3*, 95–99. [[CrossRef](#)]
13. Bhandari, U.; Zhang, C.; Yang, S. Mechanical and thermal properties of low-density Al_{20+x}Cr_{20-x}Mo_{20-y}Ti₂₀V_{20+y} alloys. *Crystals* **2020**, *10*, 278. [[CrossRef](#)]
14. Bei, H. Multi-Component Solid Solution Alloys Having High Mixing Entropy. U.S. Patent No 9,150,945, 6 October 2015.
15. Klimova, M.V.; Semenyuk, A.O.; Shaysultanov, D.G.; Salishchev, G.A.; Zhrebtsov, S.V.; Stepanov, N.D. Effect of carbon on cryogenic tensile behavior of CoCrFeMnNi-type high entropy alloys. *J. Alloy. Compd.* **2019**, *811*, 152000. [[CrossRef](#)]
16. Joo, S.H.; Kato, H.; Jang, M.J.; Moon, J.; Kim, E.B.; Hong, S.J.; Kim, H.S. Structure and properties of ultrafine-grained CoCrFeMnNi high-entropy alloys produced by mechanical alloying and spark plasma sintering. *J. Alloy. Compd.* **2017**, *698*, 591–604. [[CrossRef](#)]
17. Cheng, H.; Wang, H.Y.; Xie, Y.C.; Tang, Q.H.; Dai, P.Q. Controllable fabrication of a carbide-containing FeCoCrNiMn high-entropy alloy: Microstructure and mechanical properties. *Mater. Sci. Technol.* **2017**, *33*, 2032–2039. [[CrossRef](#)]
18. Shun, T.-T.; Du, Y.-C. Age hardening of the Al_{0.3}CoCrFeNiC_{0.1} high entropy alloy. *J. Alloy. Compd.* **2009**, *478*, 269–272. [[CrossRef](#)]
19. Velo, I.L.; Gotor, F.J.; Alcalá, M.D.; Real, C.; Córdoba, J.M. Fabrication and characterization of WC-HEA cemented carbide based on the CoCrFeNiMn high entropy alloy. *J. Alloy. Compd.* **2018**, *746*, 1–8. [[CrossRef](#)]
20. Guo, N.N.; Wang, L.; Luo, L.S.; Li, X.Z.; Chen, R.R.; Su, Y.Q.; Guo, J.J.; Fu, H.Z. Microstructure and mechanical properties of in-situ MC-carbide particulates-reinforced refractory high-entropy Mo_{0.5}NbHf_{0.5}ZrTi matrix alloy composite. *Intermetallics* **2016**, *69*, 74–77. [[CrossRef](#)]
21. Wu, Z.; Wang, C.; Zhang, Y.; Feng, X.; Gu, Y.; Li, Z.; Jiao, H.; Tan, X.; Xu, H. The AC Soft Magnetic Properties of FeCoNi_xCuAl (1.0 ≤ x ≤ 1.75) High-Entropy Alloys. *Mater. Res. Lett.* **2019**, *12*, 4222. [[CrossRef](#)]

22. Li, J.; Gao, B.; Wang, Y.; Chen, X.; Xin, Y.; Tang, S.; Liu, B.; Liu, Y.; Song, M. Microstructures and mechanical properties of nano carbides reinforced CoCrFeMnNi high entropy alloys. *J. Alloy. Compd.* **2019**, *792*, 170–179. [[CrossRef](#)]
23. Yan, J.; Knight, J.; Kunz, M.; Vennila Raju, S.; Chen, B.; Gleason, A.E.; Godwal, B.K.; Geballe, Z.; Jeanloz, R.; Clark, S.M. The resistive-heating characterization of laser heating system and LaB₆ characterization of X-ray diffraction of beamline 12.2.2 at advanced light source. *J. Phys. Chem. Solids* **2010**, *71*, 1179–1182. [[CrossRef](#)]
24. Bassett, W.A. Diamond anvil cell, 50th birthday. *High Press. Res.* **2009**, *29*, 163–186. [[CrossRef](#)]
25. Kunz, M.; Yan, J.; Cornell, E.; Domning, E.E.; Yen, C.E.; Doran, A.; Beavers, C.M.; Treger, A.; Williams, Q.; MacDowell, A.A. Implementation and application of the peak scaling method for temperature measurement in the laser heated diamond anvil cell. *Rev. Sci. Instrum.* **2018**, *89*, 083903. [[CrossRef](#)]
26. Raju, S.V.; Zaug, J.M.; Chen, B.; Yan, J.; Knight, J.W.; Jeanloz, R.; Clark, S.M. Determination of the variation of the fluorescence line positions of ruby, strontium tetraborate, alexandrite, and samarium-doped yttrium aluminum garnet with pressure and temperature. *J. Appl. Phys.* **2011**, *110*, 023521. [[CrossRef](#)]
27. Pasternak, S.; Aquilanti, G.; Pascarelli, S.; Poloni, R.; Canny, B.; Coulet, M.-V.; Zhang, L. A diamond anvil cell with resistive heating for high pressure and high temperature X-ray diffraction and absorption studies. *Rev. Sci. Instrum.* **2008**, *79*, 085103. [[CrossRef](#)]
28. Bhandari, U.; Zhang, C.; Zeng, C.; Guo, S.; Yang, S. Computational and experimental investigation of refractory high entropy alloy Mo₁₅Nb₂₀Re₁₅Ta₃₀W₂₀. *J. Mater. Res. Technol.* **2020**, *9*, 8929–8936. [[CrossRef](#)]
29. Yan, J.; Yang, S. An Alternative Thermal Equation of State for Solids at High Temperature High Pressure. *Submitted to Minerals*, under revision.
30. Prescher, C.; Prakapenka, V.B. DIOPTAS: A program for reduction of two-dimensional X-ray diffraction data and data exploration. *High Press. Res.* **2015**, *35*, 223–230. [[CrossRef](#)]
31. Rietveld, H.M. A profile refinement method for nuclear and magnetic structures. *J. Appl. Crystallogr.* **1969**, *2*, 65–71.
32. Bragg, W.H.; Bragg, W.L. The reflection of X-rays by crystals. *Proc. R. Soc. Lond. Ser. A Contain. Pap. Math. Phys. Character* **1913**, *88*, 428–438. [[CrossRef](#)]
33. Yao, H.W.; Qiao, J.W.; Hawk, J.A.; Zhou, H.F.; Chen, M.W.; Gao, M.C. Mechanical properties of refractory high-entropy alloys: Experiments and modeling. *J. Alloy. Compd.* **2017**, *696*, 1139–1150. [[CrossRef](#)]
34. Altomare, A.; Corriero, N.; Cuocci, C.; Falcicchio, A.; Moliterni, A.; Rizzi, R. Main features of QUALX2.0 software for qualitative phase analysis. *Powder Diffr.* **2017**, *32*, S129–S134. [[CrossRef](#)]
35. Shivam, V.; Basu, J.; Pandey, V.K.; Shadangi, Y.; Mukhopadhyay, N.K. Alloying behaviour, thermal stability and phase evolution in quinary AlCoCrFeNi high entropy alloy. *Adv. Powder Technol.* **2018**, *29*, 2221–2230. [[CrossRef](#)]
36. Takeuchi, A.; Inoue, A. Classification of bulk metallic glasses by atomic size difference, heat of mixing and period of constituent elements and its application to characterization of the main alloying element. *Mater. Trans.* **2005**, *46*, 2817–2829. [[CrossRef](#)]
37. Bale, C.W.; Bélisle, E.; Chartrand, P.; Deckerov, S.A.; Eriksson, G.; Gheribi, A.E.; Hack, K.; Jung, I.H.; Kang, Y.B.; Melançon, J.; et al. FactSage thermochemical software and databases, 2010–2016. *Calphad* **2016**, *54*, 35–53. [[CrossRef](#)]
38. Rubinovich, L.; Polak, M. Site-specific segregation and compositional ordering in Ni-based ternary alloy nanoclusters computed by the free-energy concentration expansion method. *Phys. Rev. B* **2004**, *69*, 155405. [[CrossRef](#)]
39. Polak, M.; Rubinovich, L. Stabilization and transformation of asymmetric configurations in small-mismatch alloy nanoparticles: The role of coordination dependent energetics. *Phys. Chem. Chem. Phys.* **2014**, *16*, 1569–1575. [[CrossRef](#)]
40. Yamamoto, Y.; Brady, M.P.; Lu, Z.P.; Maziasz, P.J.; Liu, C.T.; Pint, B.A.; More, K.L.; Meyer, H.M.; Payzant, E.A. Creep-resistant, Al₂O₃-forming austenitic stainless steels. *Science* **2007**, *316*, 433. [[CrossRef](#)]

